



## Supporting Information

for *Small*, DOI: 10.1002/smll.202104946

Reusable Cavitand-Based Electrospun Membranes for the Removal of Polycyclic Aromatic Hydrocarbons from Water

*Mattia Amorini, Nicolò Riboni, Lucia Pesenti, Valentina Antonia Dini, Alessandro Pedrini, Chiara Massera, Chiara Gualandi, Federica Bianchi, Roberta Pinalli,\* and Enrico Dalcanale\**

## Table of contents

1	<i>General experimental methods</i> .....	S2
2	<i>PAHs structures</i> .....	S5
3	<i>Experimental procedures</i> .....	S6
4	<i>BenzoQxCav characterization</i> .....	S8
5	<i>Crystallographic determination of BenzoQxCav structure</i> .....	S10
6	<i>Cavity computational study</i> .....	S12
7	<i>TGA analysis of BenzoQxCav</i> .....	S13
8	<i>Calculation of the dimensions of PAH micropollutants</i> .....	S13
9	<i>ATR-IR analysis of PAN-BenzoQxCav membrane</i> .....	S16
10	<i>Fluorescence emission of electrospun PAN membranes</i> .....	S17
11	<i>Filtering system Set-up</i> .....	S18
12	<i>Adsorption Kinetics</i> .....	S18
13	<i>Vase-Kite equilibrium of BenzoQxCav in solution</i> .....	S20
14	<i>SEM analysis of PAN-BenzoQxCav after use and regeneration</i> .....	S26
15	<i>Regeneration and reuse of the pristine PAN electrospun membranes</i> .....	S27
16	<i>References</i> .....	S27

# 1 General experimental methods

## Synthesis

Unless stated otherwise, all reactions were carried out using strictly anhydrous conditions under Ar atmosphere. All solvents were dried and distilled using standard procedures. All commercially obtained reagents were used as received unless otherwise specified. Silica column chromatography was performed using silica gel (Fluka 230 – 400 mesh). **Resorcinarene** [ $C_6H_{13}$ , **H**]<sup>[1]</sup> and 2,3-dichlorobenzo[g]quinoxaline (**1**)<sup>[2]</sup> were prepared according to published procedures.

## NMR spectroscopy

NMR spectra were collected on Bruker Avance 400 (400 MHz) spectrometer at 25 °C. <sup>1</sup>H and <sup>13</sup>C NMR chemical shifts ( $\delta$ ) are given in part per million (ppm) and calibrated to either residual solvent signal. NMR data are reported in the following format: chemical shift (multiplicity (s = singlet, d = doublet, t = triplet, q = quartet, dd = doublet of doublets, m = multiplet), coupling constants (Hz), integration).

## Mass spectrometry

Electrospray ionization mass spectrometry (ESI-MS) experiments were performed using a Waters ZMD spectrometer equipped with an electrospray interface. High-resolution MALDI-TOF was performed using an AB SCIEX MALDI TOF-TOF 4800 Plus (matrix:  $\alpha$ -cyano-4-hydroxycinnamic acid).

## UV-Vis absorption and fluorescence spectroscopy

Optical measurements were performed on Thermo Scientific™ Evolution™ 260 Bio UV-Vis spectrophotometer and on Horiba Jobin-Yvon FluoroMax®-3 spectrofluorometer.

## Thermogravimetric Analysis

Measurements were performed on a Perkin Elmer TGA 8000 from 25 to 900 °C at a 10 °C/min heating rate under inert (nitrogen) atmosphere.

## Electrospinning

The electrospun mats were produced using a home-made electrospinning apparatus composed by a SL 50 P10/CE/230 high voltage power supplier (Spellman, New York, USA), a KDS-200 syringe pump (KD Scientific Inc., Massachusetts, USA), a glass syringe containing the polymer solution, a stainless-steel blunt-ended needle (inner diameter 0.51 mm, Hamilton, Bonaduz, Switzerland)

connected with the power supply electrode and a grounded cylindrical aluminum collector (length = 10 cm, diameter = 5 cm, rotating at 50 rpm). The polymer solution was ejected at a flow rate of 1 mL h<sup>-1</sup>, the needle was placed 22 cm away from the collector and the applied voltage was set at 22 kV. Unfunctionalized PAN membranes were produced from a 9% (w/v) solution of PAN dissolved in DMF. PAN-**BenzoQxCav** membranes were obtained by dissolving a proper amount of cavitand in the starting polymer solution, to achieve a final concentration of 6 wt% **BenzoQxCav** in the fibers. In a typical preparation, 270 mg of PAN and 17.23 mg of **BenzoQxCav** were dissolved in 3 mL of DMF. Electrospinning was performed at room temperature and relative humidity in the range 40-50%. Membrane thickness was in the range 180-230 μm.

### **Scanning Electron Microscopy**

Sample morphology was observed with a scanning electron microscope (SEM, Leica Cambridge Stereoscan 360) at an accelerating voltage of 20 kV. Prior to SEM analysis, the samples were sputtered with gold. The distribution of fibre diameters was determined through the measurement of about 300 fibres and the results are given as the average diameter ± standard deviation (SD). The one-way ANOVA was used to test the statistical significance of the difference between the mean values ( $p < 0.0001$ ).

### **Water contact angle**

Static contact angle measurements were performed on the electrospun membranes by using a Theta Lite tensiometer (Biolin Scientific, Sweden) under ambient conditions by recording the side profiles of deionized water drops in a time range 0-10 sec. Ten drops were observed for each sample. Results were provided as average value of contact angle (at six seconds) ± standard deviation.

### **Confocal microscope**

Confocal images were registered on a Nikon A1R microscope with a 20x objective (NA=0.90, magnification 100x), an excitation laser at 401 nm and two GaAsP PMTs with emission filter at 525/50nm and at 450/50nm.

### **Fiber preparation and SPME extraction**

**BenzoQxCav** coated silica fibers were obtained by dipping the silica support of commercially available fibers (1 cm length) in an epoxy glue and, after 2 min, in the **BenzoQxCav** powder.

The extraction performance of the **BenzoQxCav** coating was tested by dipping the fiber into a water solution spiked with the 16 PAH pollutants (US Environmental Protection Agency (EPA) 525 PAH

Mix B, 500  $\mu\text{g ml}^{-1}$  each component in acetone) each at 100  $\text{ng L}^{-1}$  for 45 minutes at 60°C. Then, the fibers were thermally desorbed in the GC injection port at 270°C for 2 min.

### **Water analysis**

10 mL of water sample spiked with the 16 EPA PAHs each at 100  $\text{ng L}^{-1}$  were filtered using both unfunctionalized and functionalized membranes. A constant filtration flux (0.16  $\text{mL s}^{-1}$ ) was applied to a frit-type filter (Millipore Swinney Stainless 13 mm filter) containing the membranes. The PAHs residual concentration in the filtered water was assessed by SPME-GC-MS analysis using a PDMS-30 $\mu\text{m}$  fiber. PAHs extraction was carried out using the direct immersion mode for 45 minutes at 60°C. Subsequently, the fiber was desorbed at 270°C and the resulting aromatic hydrocarbons analyzed by GC-MS (n=3).

### **Regeneration procedure**

The used membranes were regenerated applying a constant flux (0.16  $\text{mL s}^{-1}$ ) of: (i) 30 mL of a TFA aqueous solution (pH = 1.5), (ii) water till neutral pH (20 mL total); (iii) 20 mL of a  $\text{NH}_3$  aqueous solution (pH = 10); (iv) water till neutral pH (20 mL total).

### **GC-MS analysis**

A HP 6890 Series Plus gas chromatograph (Agilent Technologies, Milan, Italy) coupled to a MSD 5973 mass spectrometer (Agilent Technologies) and equipped with a PAL Combi-xt autosampler (CTC Analytics AG, Switzerland) was used for PAHs determination. Chromatographic separation was carried out on a 30 m  $\times$  0.25 mm i.d, 0.25  $\mu\text{m}$  film thickness Rxi-5Sil MS capillary column (Restek, Bellefonte, PA, USA), using helium as carrier gas at a constant flow rate of 1.0  $\text{ml min}^{-1}$ . The following GC oven temperature program was used: 70°C; 15°C  $\text{min}^{-1}$  to 290 °C (held for 4 min). The mass spectrometer was operated with an electron ionization (EI) ion source using an electron energy of 70 eV. A solvent delay time of 1 min was applied. The transfer line and the ion source were maintained at 280°C and 150°C, respectively. The mass spectrometer was operated in time scheduled selected-ion monitoring mode by recording the current of the following ions:  $m/z$  128, 127 and 102 for naphthalene from 1 to 5.5 min;  $m/z$  152, 151 and 76 for acenaphthylene and  $m/z$  154, 153 and 76 for acenaphthene from 5.5 to 7.6 min;  $m/z$  166, 165 and 139 for fluorene from 7.6 to 8.5 min;  $m/z$  178, 176 and 152 for phenanthrene and anthracene from 8.5 to 10.5 min;  $m/z$  202, 200 and 101 for pyrene and fluoranthene from 10.5 to 12.5 min;  $m/z$  228, 226 and 113 for benzo[*a*]anthracene and chrysene from 12.5 to 14.5 min;  $m/z$  252, 253 and 126 for benzo[*b*]fluoranthene, benzo[*k*]fluoranthene and benzo[*a*]pyrene from 14.5 to 16.5 min;  $m/z$  279, 278, 276, 277, 139 and

138 for benzo[*ghi*]perylene, dibenzo[*a,h*]anthracene and indeno[1,2,3-*cd*]pyrene from 16.5 to 19.2 min. For all the investigated analytes the corresponding ion ratios were used for confirmation purposes. A dwell time of 30ms was used for all the ions. All the analyses were performed by setting the electron multiplier voltage at 960 V. Signal acquisition and data processing were performed using the HP Chemstation (Agilent Technologies).

## 2 PAHs structures

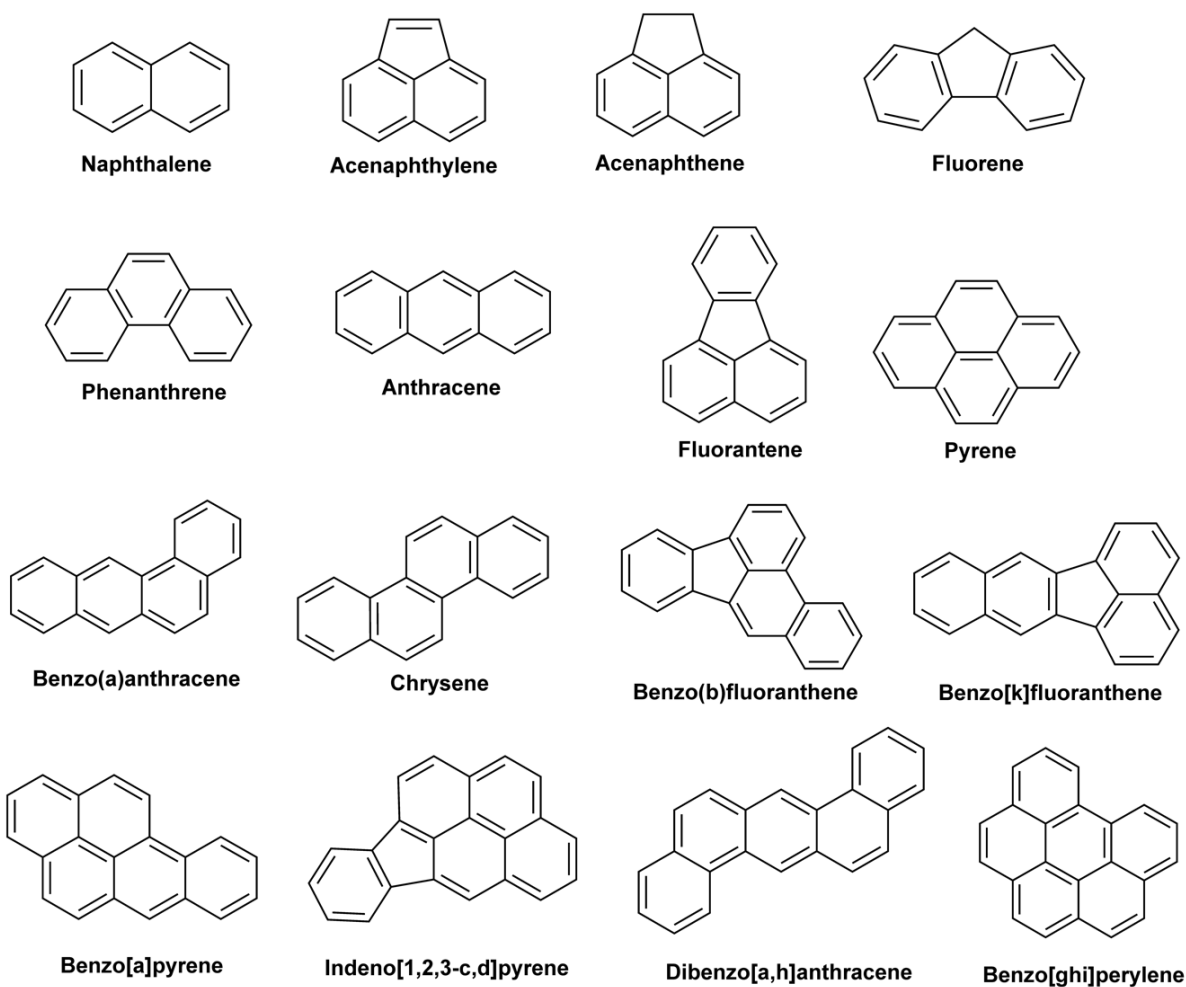
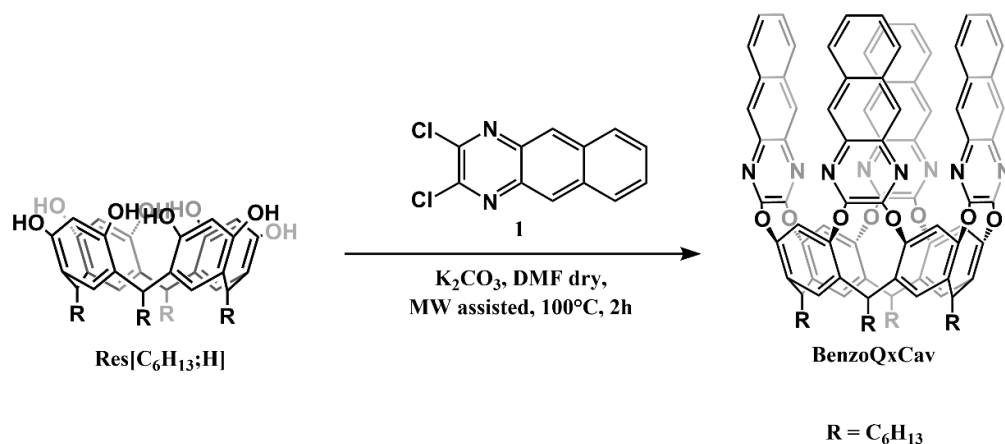


**Chart S1.** Structures of the 16 PAHs involved in the study.

### 3 Experimental procedures



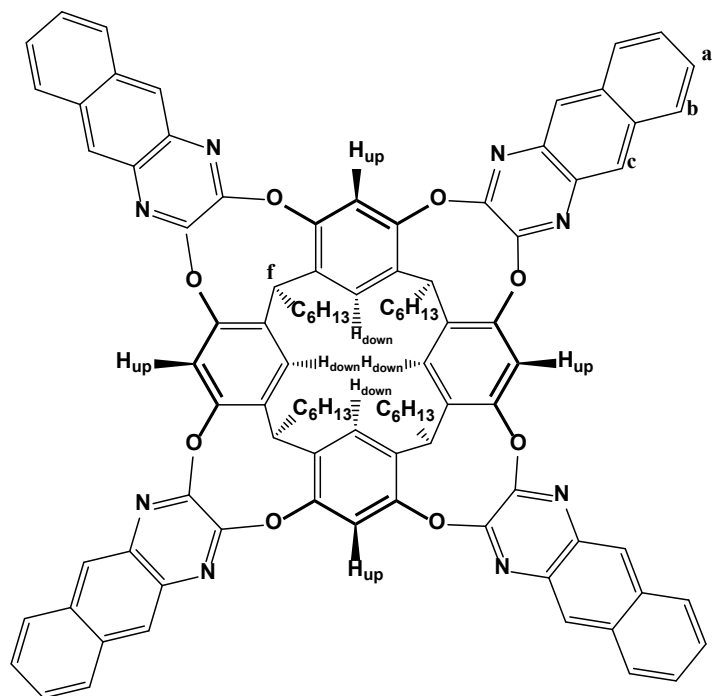
**Scheme S1.** Benzoquinoxaline cavitand (**BenzoQxCav**) synthesis.

#### Benzoquinoxaline cavitand (**BenzoQxCav**)

To a solution of **Resorcinarene** [ $\text{C}_6\text{H}_{13}$ ; **H**] (0.075 g, 0.091 mmol) in dry DMF (3 mL) in an oven-dried microwave vessel,  $\text{K}_2\text{CO}_3$  (0.126 g, 0.912 mmol) was added. The resulting mixture was stirred for 5 minutes at room temperature in inert atmosphere, followed by addition of **2,3-dichlorobenzo[g]quinoxaline 1** (0.1 g, 0.401 mmol). The mixture was stirred at  $100^\circ\text{C}$  under microwave irradiation for 2 hours. The reaction was quenched by pouring in acidic water (10 mL) and the resulting precipitate was filtered, washed with water and dried under reduced pressure. The crude was purified by crystallization from ethyl acetate/chloroform (8:2) to give **BenzoQxCav** as a yellowish solid (120 mg, 0.078 mmol, 86%).

$^1\text{H}$  NMR (400 MHz,  $\text{CDCl}_3$ ,  $25^\circ\text{C}$ ):  $\delta$  = 8.24 (s, 8H,  $\text{H}_c$ ), 8.18 (s, 4H,  $\text{ArH}_{\text{up}}$ ), 7.72 (dd,  $J_o(\text{H,H}) = 6.5$  Hz,  $J_m(\text{H,H}) = 3.3$  Hz, 8H,  $\text{H}_b$ ), 7.37 (dd,  $J_o(\text{H,H}) = 6.6$  Hz,  $J_m(\text{H,H}) = 3.2$  Hz, 8H,  $\text{H}_a$ ), 7.22 (s, 4H,  $\text{ArH}_{\text{down}}$ ), 5.49 (t,  $^3J(\text{H,H}) = 8.0$  Hz, 4H,  $\text{ArCH}_f$ ), 2.35 – 2.20 (m, 8H,  $\text{CHCH}_2\text{CH}_2$ ), 1.54 – 1.21 (m, 32H,  $\text{CH}_2$ ), 0.98 – 0.85 (m, 12H,  $\text{CH}_2\text{CH}_3$ )

(Assignment by COSY NMR).



$^{13}C$  NMR (101 MHz,  $CDCl_3$ ,  $25^\circ C$ )  $\delta$  152.79, 137.04, 135.81, 134.29, 133.47, 128.41, 126.91, 126.34, 123.78, 118.87, 77.80, 77.48, 77.16, 35.09, 32.76, 32.33, 29.82, 28.34, 23.14, 14.54.

MALDI-TOF calculated for  $C_{100}H_{89}N_8O_8$   $[M+H]^+$   $m/z$ : 1530.6836, found  $m/z$ : 1530.6887.



## 4 BenzoQxCav characterization

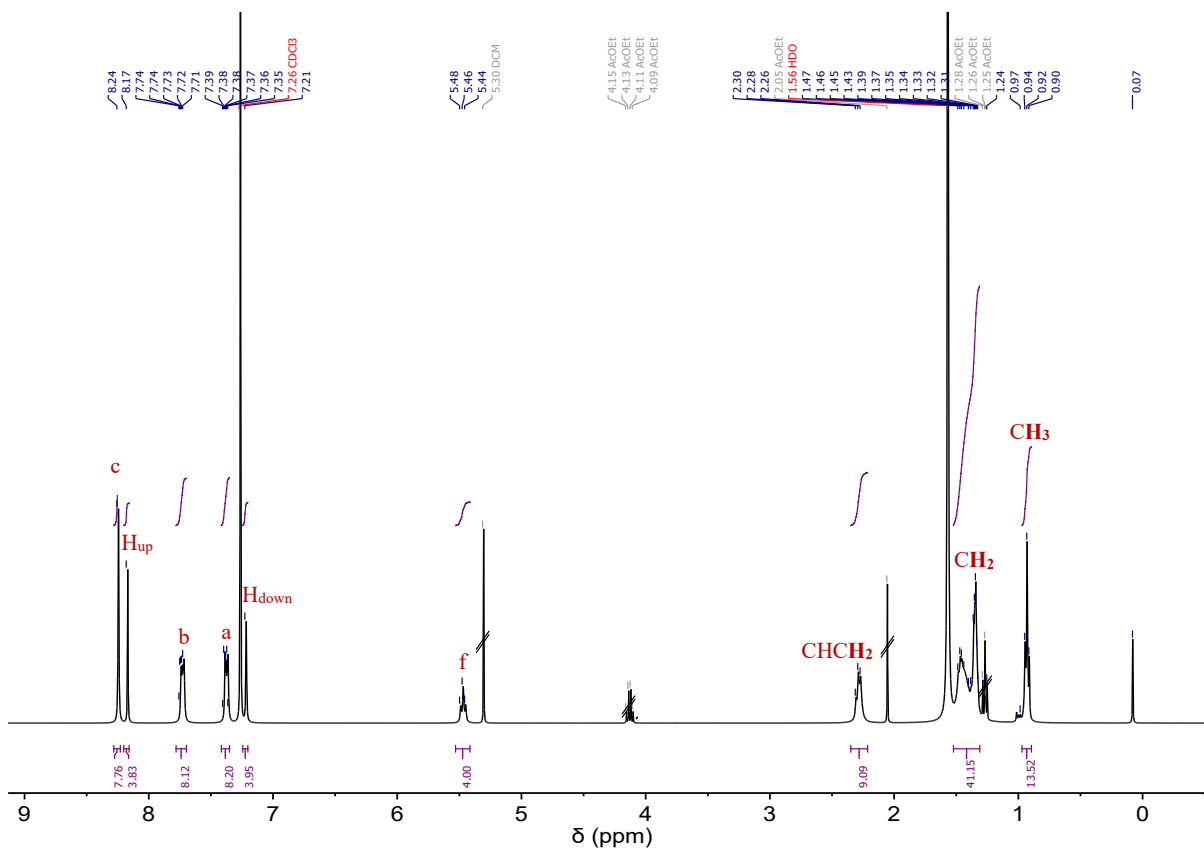
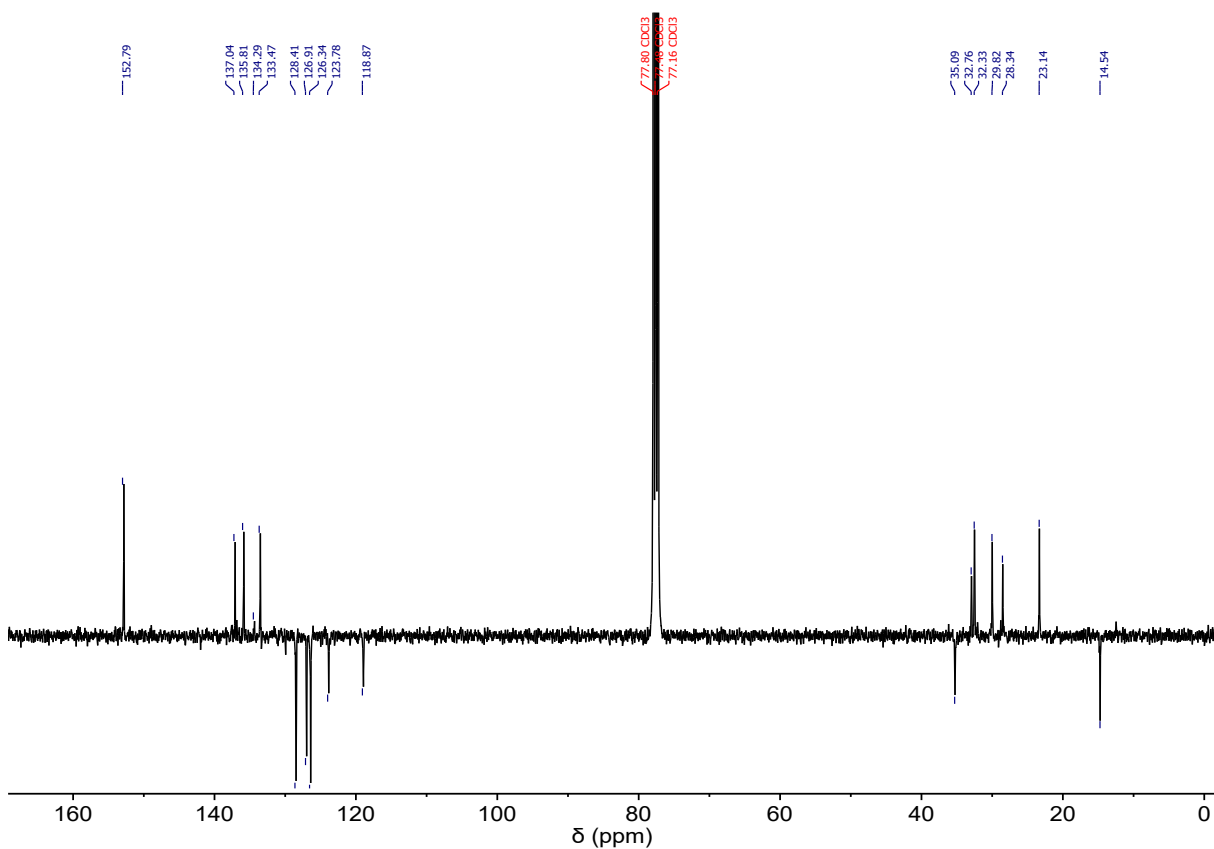
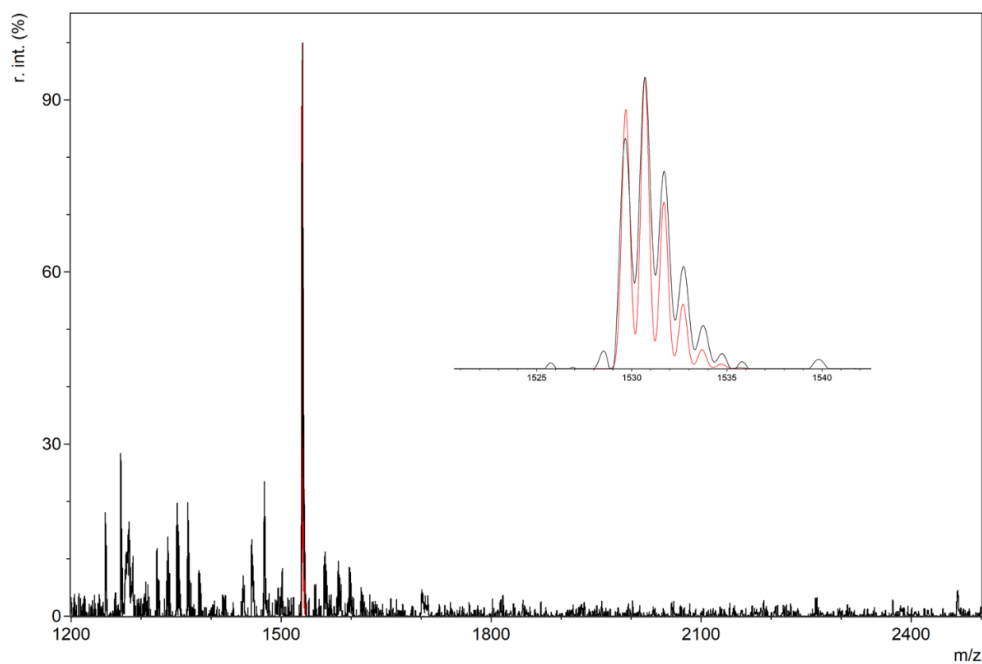


Figure S1. <sup>1</sup>H NMR (400 MHz) spectrum of BenzoQxCav in CDCl<sub>3</sub> at 25 °C.



**Figure S2.** APT  $^{13}\text{C}$  NMR (100 MHz) spectrum of **BenzoQxCav** in  $\text{CDCl}_3$  at 25 °C (CH and  $\text{CH}_3$  negative signals,  $\text{CH}_2$  and C positive signals).



**Figure S3.** MALDI-TOF spectrum of **BenzoQxCav**, with experimental (black lines) versus theoretical (red) isotopic distribution pattern in the inset.

## 5 Crystallographic determination of BenzoQxCav structure

The crystal structure of **BenzoQxCav** was determined by X-ray diffraction methods. Crystal data and experimental details for data collection and structure refinement are reported in Table S1.

Intensity data and cell parameters were recorded at 190(2) K on a Bruker ApexII diffractometer equipped with a CCD area detector, using MoK $\alpha$  radiation ( $\lambda = 0.71073$  Å). The raw frame data were processed using the programs SAINT and SADABS.<sup>[3]</sup> The structure was solved by Direct Methods using the SIR97 program<sup>[4]</sup> and refined on  $F_o^2$  by full-matrix least-squares procedures, using the SHELXL-2014/7 program<sup>[5]</sup> in the WinGX suite v.2014.1.<sup>[6]</sup> All non-hydrogen atoms were refined with anisotropic atomic displacements, with the exception of some atoms belonging to the disordered DMF solvent molecules. The carbon-bound H atoms were placed in calculated positions and refined isotropically using a riding model with C-H ranging from 0.95 to 0.99 Å and Uiso(H) set to 1.2/1.5Ueq(C). The weighting scheme used in the last cycle of refinement was  $w = 1 / [\sigma^2 F_o^2 + (0.20000P)^2]$  where  $P = (F_o^2 + 2F_c^2)/3$ . The structure has been deposited in the Cambridge Crystallographic Data Centre as no. CCDC-2110603.

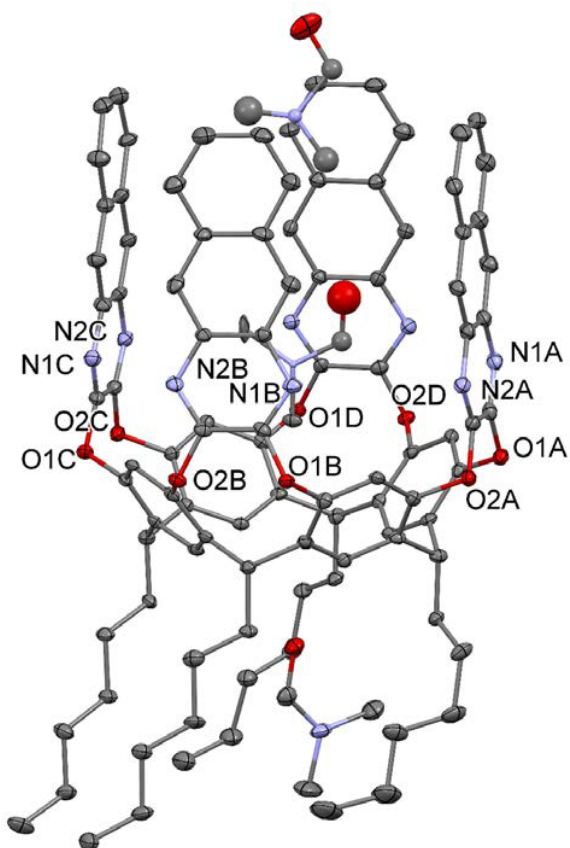


**Figure S4.** Ortep view of **BenzoQxCav** with ellipsoids drawn at the 20% level. H atoms have been omitted for clarity. The two DMF molecules inside the cavity have occupancy of 0.5 each.

**Table S1. Crystal data and structure refinement information for BenzoQxCav.**

Compound	BenzoQxCav
empirical formula	C <sub>106</sub> H <sub>102</sub> N <sub>10</sub> O <sub>10</sub>
<i>M</i>	1675.97
crys syst	Monoclinic
space group	<i>P</i> 2 <sub>1</sub> / <i>n</i>
<i>a</i> /Å	12.654(2)
<i>b</i> /Å	18.061(2)
<i>c</i> /Å	40.271(5)
$\beta$ /°	98.366(7)
<i>V</i> /Å <sup>3</sup>	9106(2)
<i>Z</i>	4
<i>T</i> /K	190(2)
$\rho$ /g cm <sup>-3</sup>	1.223
$\mu$ /mm <sup>-1</sup>	0.079
<i>F</i> (000)	3552
total reflections	73502
unique reflections ( <i>R</i> <sub>int</sub> )	14232 (0.2085)
observed reflections	5641
$[F_o > 4\sigma(F_o)]$	
GOF on <i>F</i> <sup>2a</sup>	1.000
<i>R</i> indices $[F_o > 4\sigma(F_o)]^b R_1, wR_2$	0.1120, 0.2833
largest diff. peak and hole (eÅ <sup>-3</sup> )	1.197, -0.398

<sup>a</sup>Goodness-of-fit  $S = [\sum w(F_o^2 - F_c^2)^2 / (n-p)]^{1/2}$ , where *n* is the number of reflections and *p* the number of parameters. <sup>b</sup> $R_1 = \sum ||F_o| - |F_c|| / \sum |F_o|$ ,  $wR_2 = [\sum [w(F_o^2 - F_c^2)^2] / \sum [w(F_o^2)^2]]^{1/2}$ .

## 6 Cavity computational study

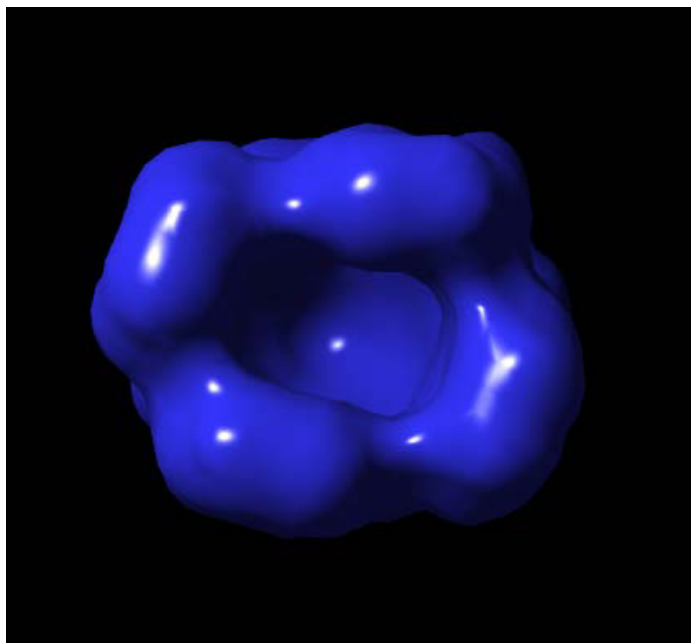


**Figure S5.** Top view of **BenzoQxCav** molecular surface computed by Yasara software.

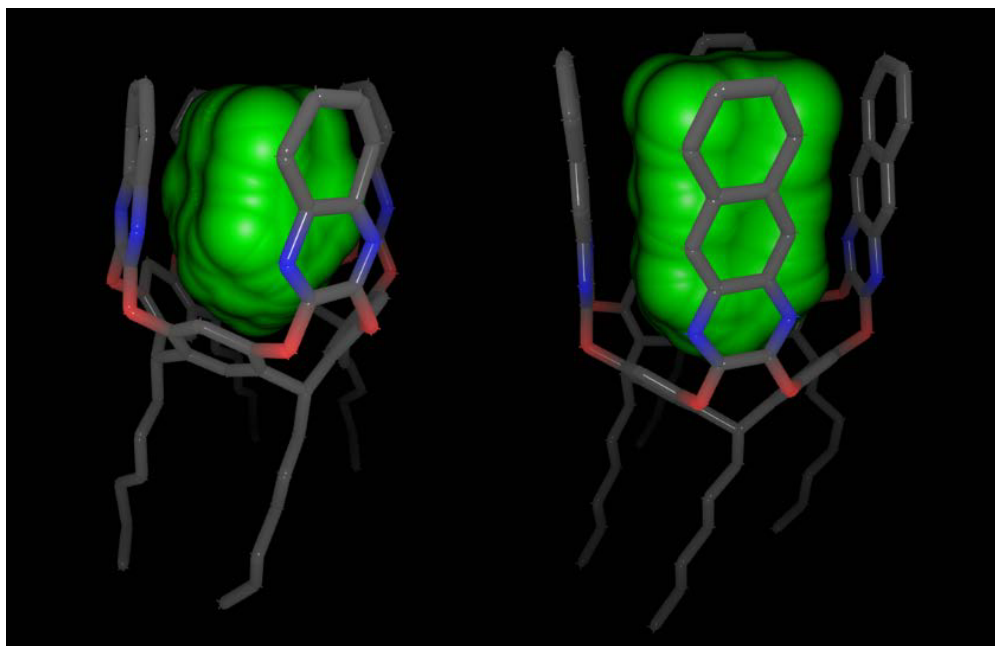


**Figure S6.** Accessible free volume inside the cavity of **QxCav** (left side) and **BenzoQxCav** (right side) calculated by Caver computational software.

## 7 TGA analysis of BenzoQxCav

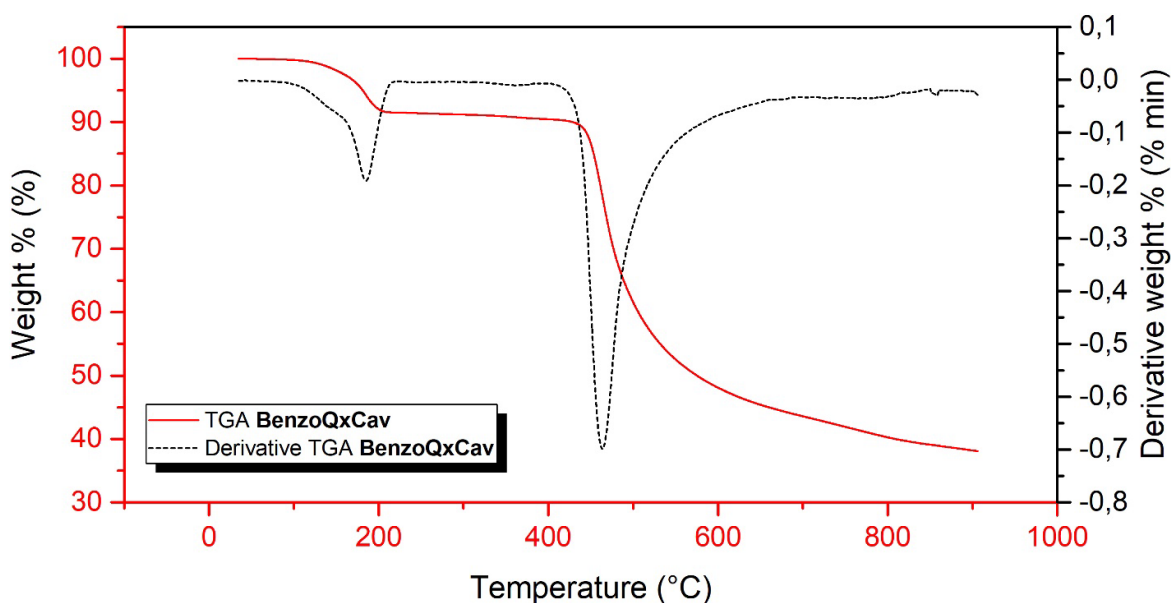


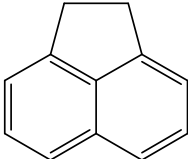
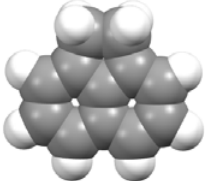
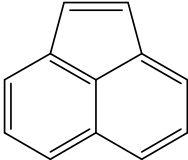
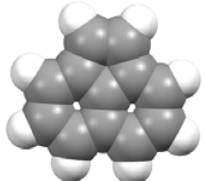
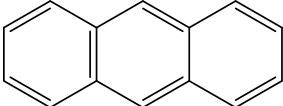
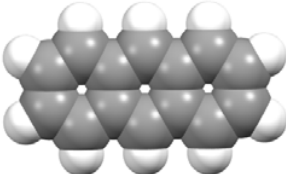
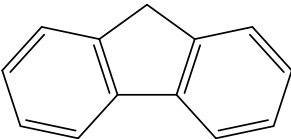
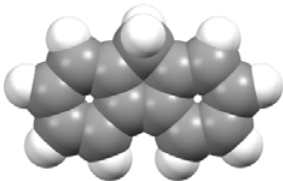
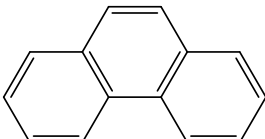
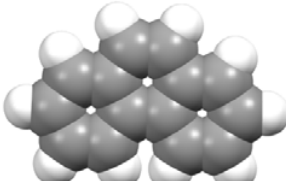
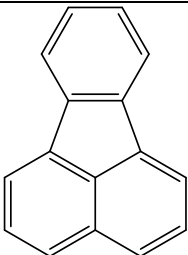
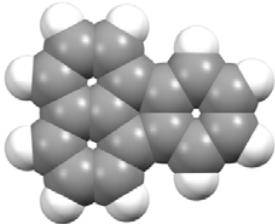
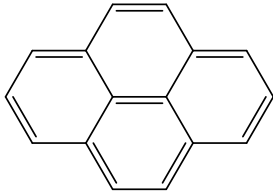
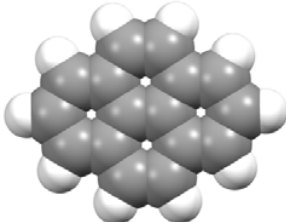
**Figure S7.** TGA analysis of **BenzoQxCav** in nitrogen. (Temperature range 25°C – 900°C, heating rate 10°C min<sup>-1</sup>).

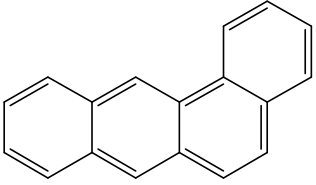
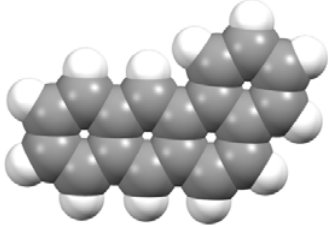
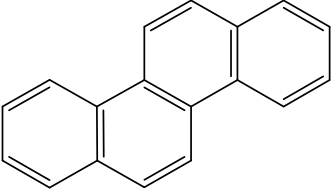
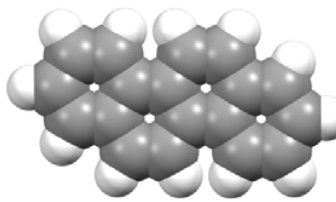
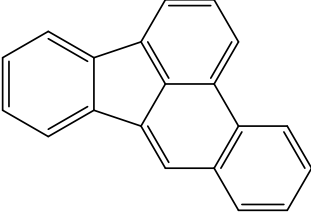
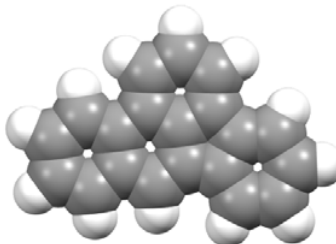
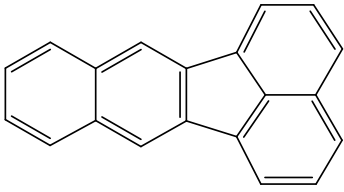
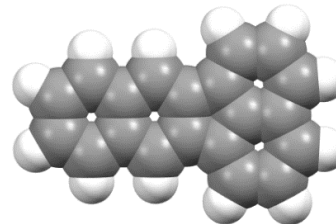
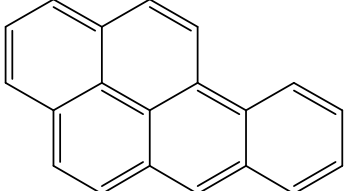
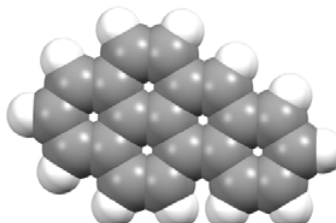
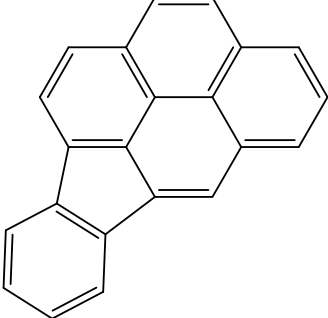
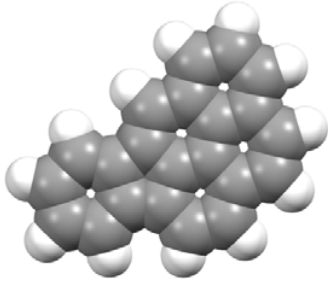
## 8 Calculation of the dimensions of PAH micropollutants

The size of the micropollutants was estimated by density functional theory (DFT) calculations and modelled using Mercury 2020. All the molecular structures are displayed in space-filling style.

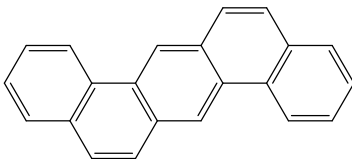
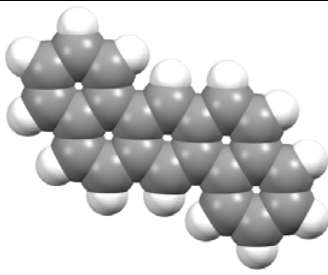
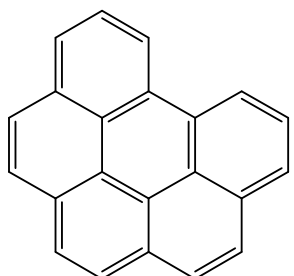
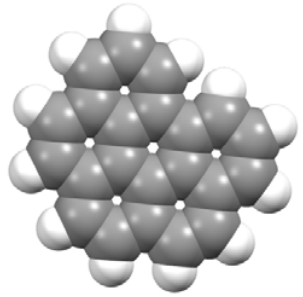
**Table S2.** Dimensions of PAHs were obtained through ground-state geometry optimized structures using density functional theory (DFT) at B3LYP/6-31G (d,p) level (gray: carbon; white: hydrogen).

PAH	MW	Chemical Structure	3D Molecular Structure	Dimension (Å) ( <i>a</i> × <i>b</i> , <i>a</i> is the long end and <i>b</i> is the short end)
Naphthalene	128.17			6.7 x 4.9

Acenaphthene	154.21			6.6 x 6
Acenaphthylene	152.2			6.2 x 6
Anthracene	178.23			9.2 x 5
Fluorene	166.22			9 x 5.2
Phenanthrene	178.23			9.2 x 5.6
Fluorantene	202.26			8.7 x 6.7
Pyrene	202.26			9.2 x 6.8

Benzo(a)anthracene	228.29			10.5 x 7.2
Chrysene	228.29			11.5 x 5.6
Benzo(b)fluoranthene	252.32			11.5 x 7.2
Benzo[k]fluoranthene	252.32			11.2 x 6.8
Benzo(a)pyrene	252.32			11.5 x 6.8
Indeno[1,2,3-c,d]pyrene	276.34			10.2 x 9.2



Dibenzo(a,h)anthracene	278.35			11.8 x 10.5
Benzo[ghi]perylene	276.33			9.2 x 9.2

## 9 ATR-IR analysis of PAN-BenzoQxCav membrane

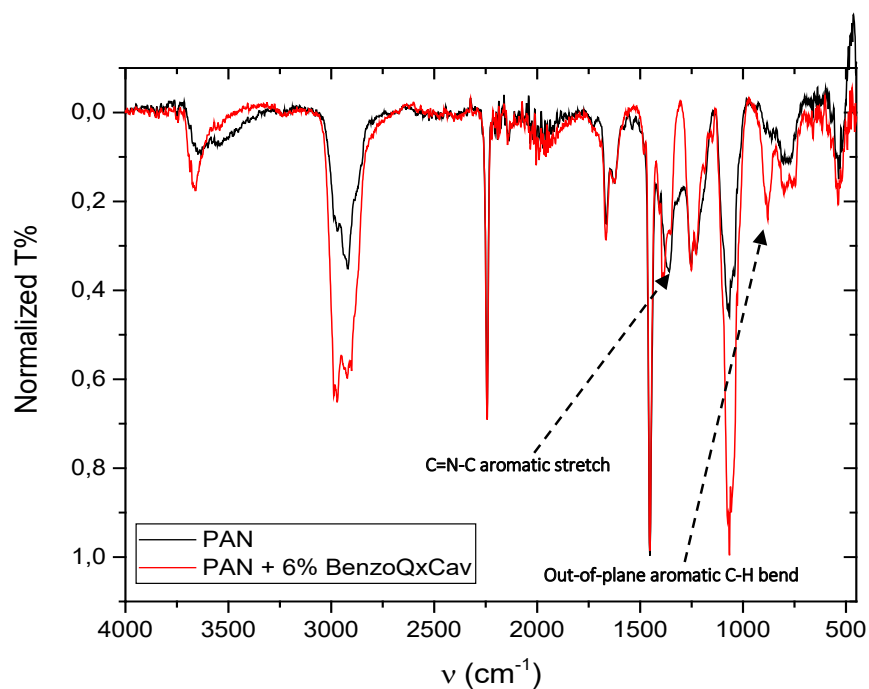


**Figure S8.** Comparison of ATR-IR spectra of electrospun PAN (black profile) and PAN + 6% BenzoQxCav (red profile) membranes.

## 10 Fluorescence emission of electrospun PAN membranes

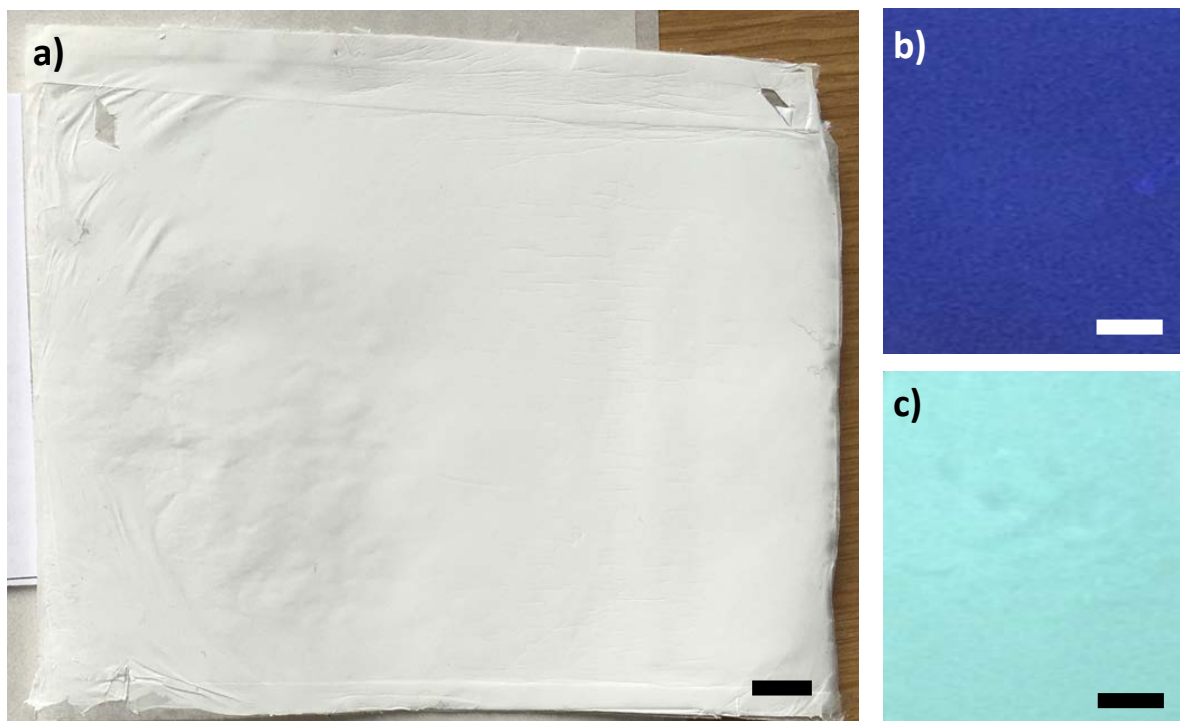


**Figure S9.** Representative picture of the electrospun membrane detached from the metallic collector (a). Reference PAN membrane (b) and PAN-**BenzoQxCav** membrane (c) under UV light (365 nm). Scale bar = 1 cm (a); 0.5 cm (b, c).

## 11 Filtering system Set-up

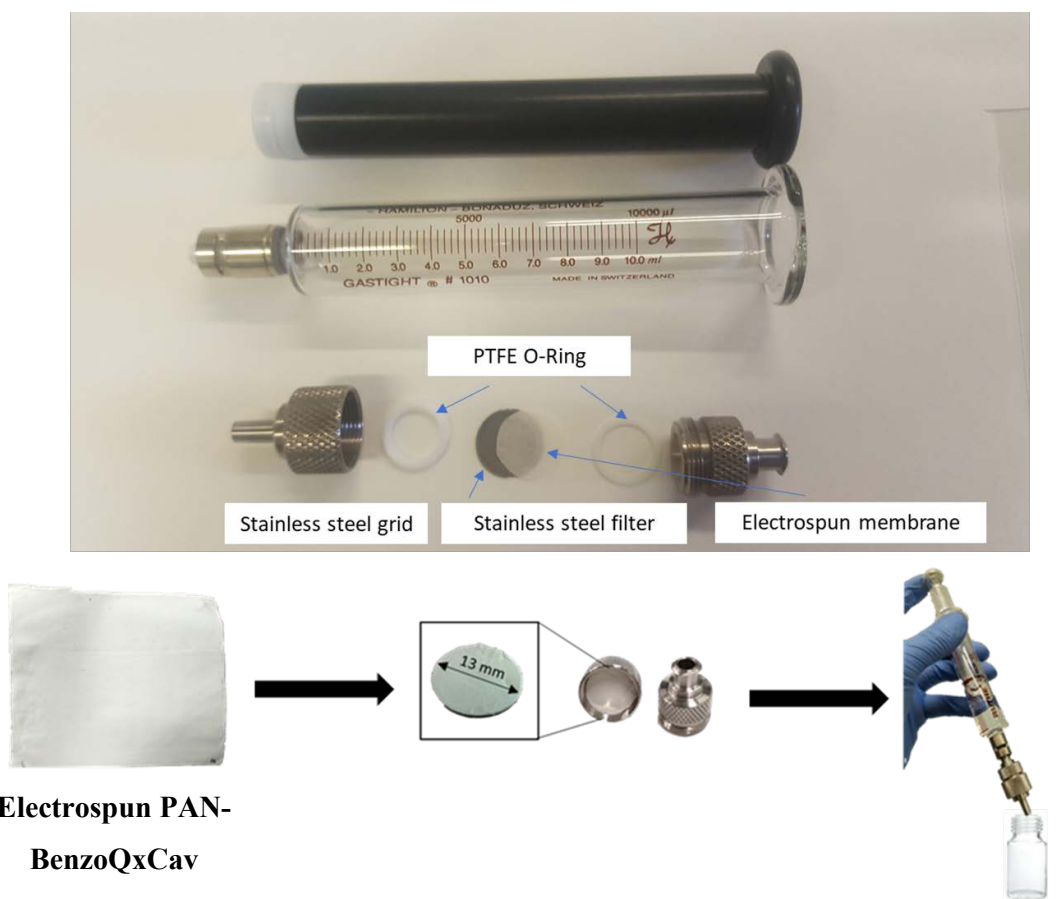


**Figure S10.** Set-up of the filtering system adopted in the purification of PAH contaminated water.

## 12 Adsorption Kinetics

The adsorption kinetics of the PAN and PAN-BenzoQxCav membrane were evaluated by analyzing water samples spiked with  $50 \mu\text{g L}^{-1}$  of each PAH. The concentration of the not adsorbed analytes along the time was determined by GC-MS analysis. The adsorption capacity of the functionalized membrane was calculated as<sup>[7,8]</sup>:

$$q_e = (C_0 - C_e) \times V/m$$

where  $C_0$  ( $\text{mg L}^{-1}$ ) is the initial concentration of PAHs,  $C_e$  is the equilibrium concentration ( $\text{mg L}^{-1}$ ),  $m$  is the mass of the adsorbent (g), and  $V$  is the solution volume (L).

Both pseudo-first-order and pseudo-second-order kinetic models were calculated as follows:

i) pseudo-first-order kinetic equation:  $\log(q_e - q_t) = \ln q_e - k_1 t/2.303$

ii) pseudo-second-order kinetic equation:  $t/q_t = 1/k_2 q_e^2 + t/q_e$

where  $q_e$  ( $\text{mg g}^{-1}$ ) is the calculated value of the adsorption capacity at equilibrium, and  $q_t$  ( $\text{mg g}^{-1}$ ) is the adsorption amount at time  $t$  (min),  $k_1$  ( $\text{min}^{-1}$ ) and  $k_2$  ( $\text{g mg}^{-1} \text{min}^{-1}$ ) are the rate constants of the pseudo-first-order and pseudo-second-order models.

The results achieved by the kinetic studies on the BenzoQxCav membrane showed that the adsorption equilibrium was reached within 180 min. Figure S11 shows the results of the sorption capacities for the functionalized and unfunctionalized membranes.

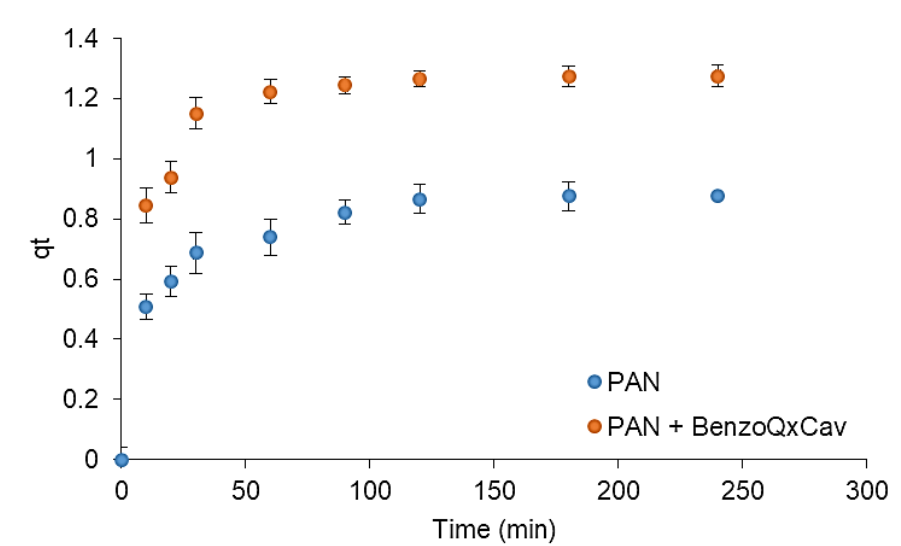


**Figure S11.** Adsorption kinetics of PAN and PAN functionalized with 6% of BenzoQxCav

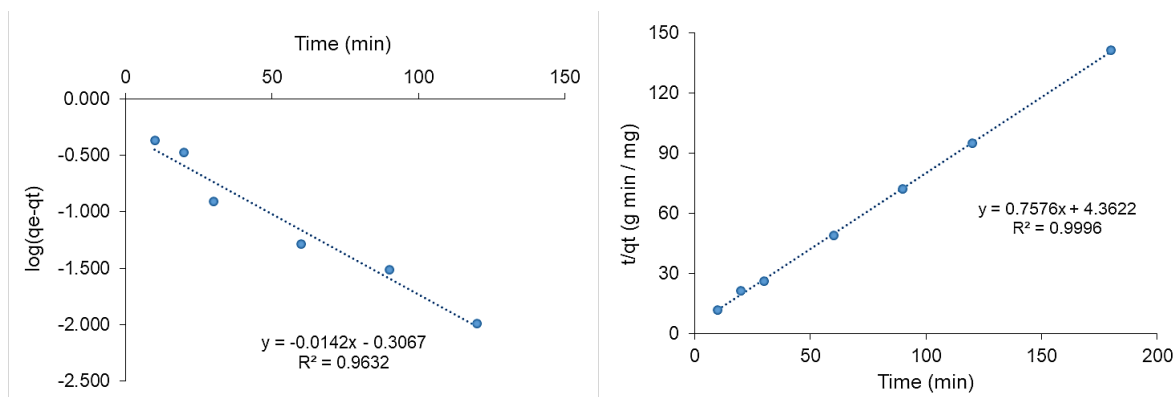


**Figure S12.** Pseudo-first-order kinetic (left) and pseudo-second-order kinetic (right) plots for PAHs removal from water.

**Table S3.** Kinetics parameters for the PAHs sorption by PAN-BenzoQxCav membrane

Experimental	Pseudo-first order model			Pseudo-second order model		
	$q_e$ ( $\text{mg g}^{-1}$ )	$k_1$ ( $\text{min}^{-1}$ )	$R^2$	$q_e$ ( $\text{mg g}^{-1}$ )	$k_2$ ( $\text{g mg}^{-1} \text{min}^{-1}$ )	$R^2$
$1.368 \pm 0.178$	$0.493 \pm 0.069$	0.0062	0.9632	$1.320 \pm 0.145$	1.32E-01	0.9996

### 13 Vase-Kite equilibrium of BenzoQxCav in solution

Depending on solvent, pH and temperature, quinoxaline-based cavitands can reversibly switch their conformation from the closed vase form, having the  $C_{4v}$  symmetry, to an open kite one, characterized by a  $C_{2v}$  symmetry and a flat extended surface. The conformational dynamics can be monitored using either  $^1\text{H-NMR}$ ,<sup>[9]</sup> fluorescence<sup>[10]</sup> or UV/Vis spectroscopy.<sup>[11]</sup>

In the case of **BenzoQxCav**, the vase-to-kite conformational switch was induced by pH perturbation and monitored using both fluorescence and UV/VIS spectroscopy. Trifluoroacetic acid (TFA) was employed to protonate the pyrazine nitrogen atoms of the benzoquinoxaline walls, inducing a Coulombic repulsion that forces the walls to open.

The UV profile of a solution of **BenzoQxCav** ( $1.9 \cdot 10^{-5}$  M) in dichloromethane (DCM) at 25 °C shows two absorption peaks at 367 and 349 nm (**Figure S13**).

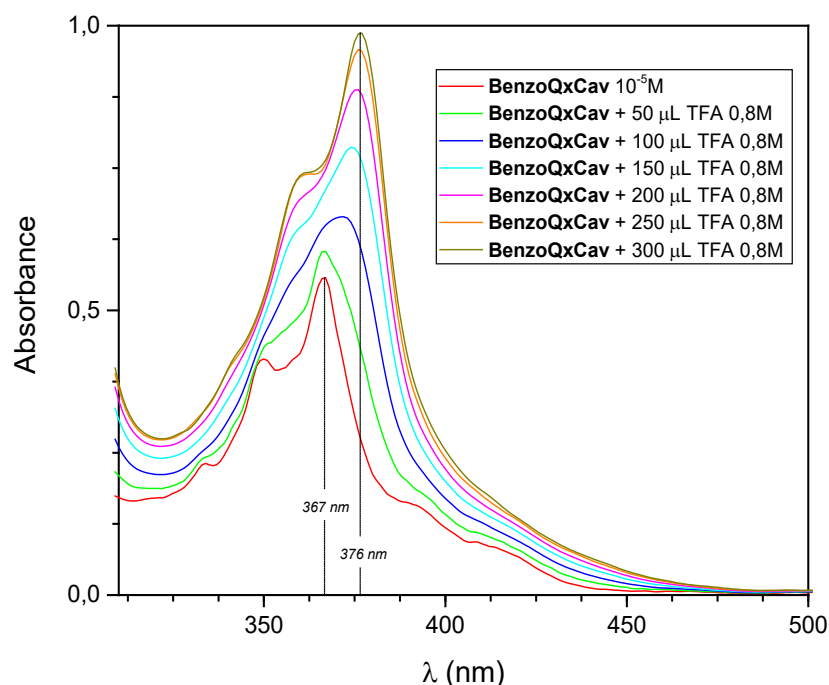


**Figure S13.** Changes of the UV absorptions of **BenzoQxCav** ( $[\text{BenzoQxCav}] = 1.9 \cdot 10^{-5}$  M) in DCM upon addition of TFA (0 - 0.23 M). T = 25 °C.

The progressive additions of TFA (50  $\mu\text{L}$  aliquots of a 0.8 M solution in DCM) to **BenzoQxCav** caused a red-shift of the absorption maximum from 367 nm to 376 nm, in agreement with literature,<sup>[9]</sup> with an increase of the molar extinction coefficient  $\epsilon$  from 28479 to 56752  $\text{M}^{-1}\text{cm}^{-1}$ . The absorption peak at 349 nm was affected by a similar bathochromic shift (from 349 nm to 359 nm) and  $\epsilon$  increase ( $\epsilon_{349} = 21230 \text{ M}^{-1} \text{ cm}^{-1}$ ;  $\epsilon_{359} = 42413 \text{ M}^{-1} \text{ cm}^{-1}$ ). Saturation was achieved at concentration of 0.23 M of TFA in DCM.

To confirm that the observed red shift is not due to a mere pH change of the solution but to the vase-to-kite conformational switch of the cavitand upon protonation of the pyrazine nitrogens, two control experiments were performed. In the first one, acetic acid, too weak to protonate the benzopyrazine nitrogens, was used to induce a pH change. As shown in **Figure S14**, the addition of acetic acid (AcOH) to a solution containing **BenzoQxCav** did not cause any shift in the UV spectrum, thus confirming that the previously observed bathochromic shift was related to the conformational switching of **BenzoQxCav** upon protonation of the benzoquinoxaline walls rather than to a change in the pH of the solution.

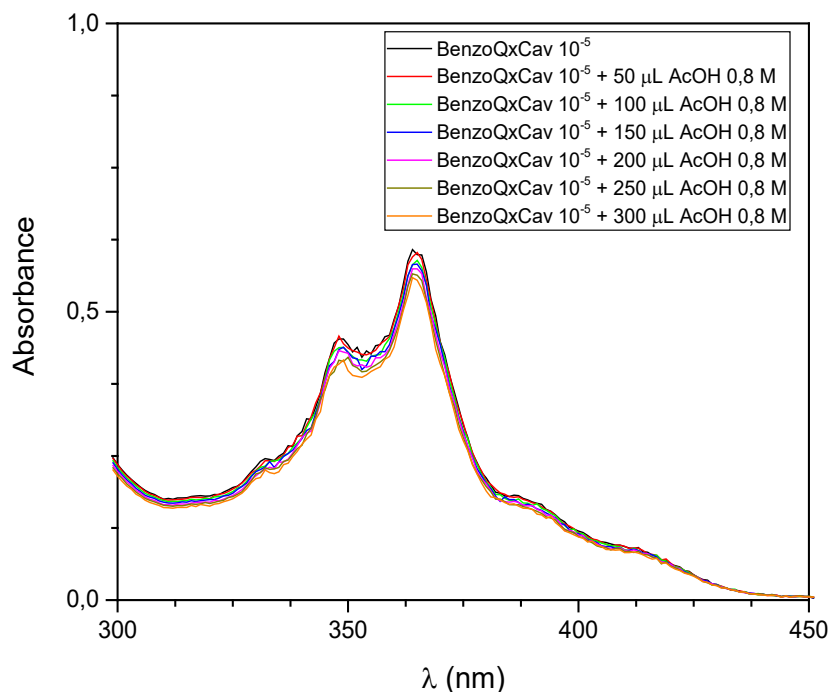


**Figure S14.** Changes of the UV absorptions of **BenzoQxCav** ( $[\text{BenzoQxCav}] = 1.9 \cdot 10^{-5} \text{ M}$ ) in DCM upon addition of AcOH (0 - 0.23 M).  $T = 25 \text{ }^\circ\text{C}$ .

The second control experiment was performed to confirm that the red shift in the UV spectrum is not due to the protonation of the pyrazine nitrogens but it is caused by the opening of the cavitand flaps. To this purpose, we added different aliquots of TFA to a solution containing exclusively the 2,3-dichlorobenzoquinoxaline bridging unit **1** and we recorded the UV spectra (**Figure S15**)

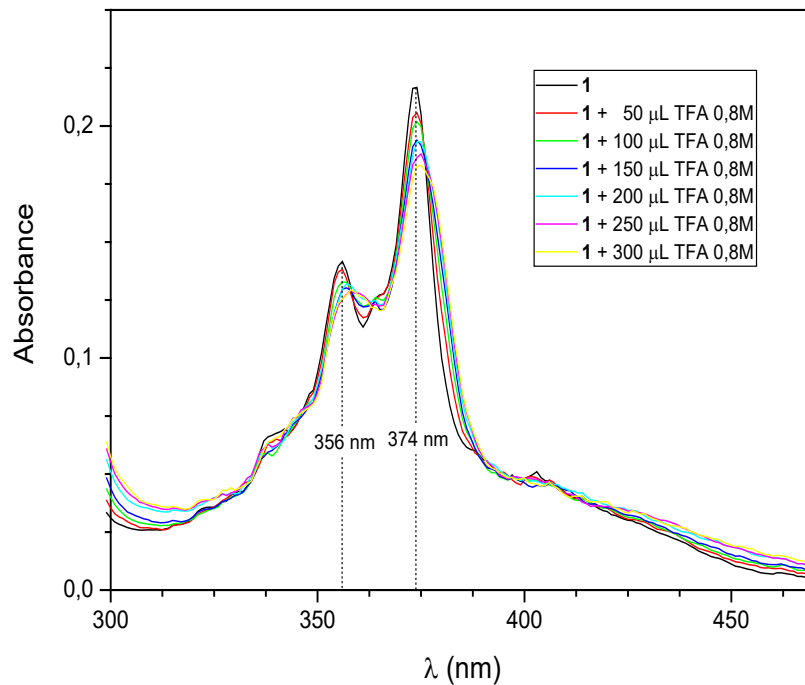


**Figure S15.** Changes of the UV absorptions of **1** ( $[1] = 1.9 \cdot 10^{-5} \text{ M}$ ) in DCM upon addition of TFA (0 - 0.23 M). T = 25 °C.

The protonation of the nitrogen atoms of **1** did not shift the absorption peaks, thus confirming that the red-shift recorded in the UV spectrum of **BenzoQxCav** upon addition of TFA is diagnostic of the vase-to-kite switch in the cavitand conformation.

The reversibility of the conformational switch in solution was monitored through UV-Vis (**Figure S16**).

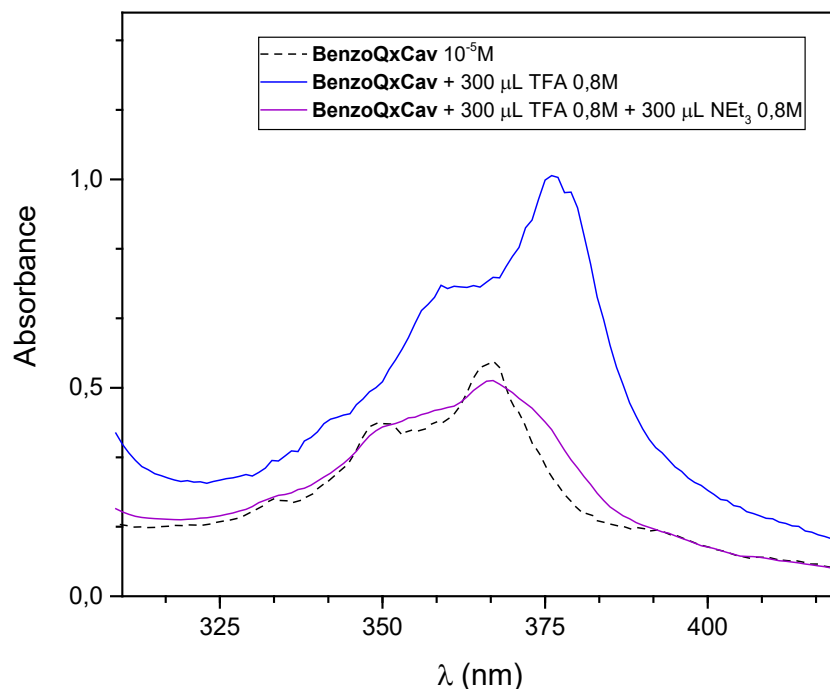


**Figure S16.** Changes of the UV absorption of **BenzoQxCav** ( $[\text{BenzoQxCav}] = 1.9 \cdot 10^{-5} \text{ M}$ ) in DCM upon addition of TFA and  $\text{NEt}_3$ .  $T = 25 \text{ }^\circ\text{C}$ .

The addition of  $\text{NEt}_3$  to a solution of **BenzoQxCav** in the kite form causes the immediate closure of the wings, and the return of the cavitaund to the vase form. This conformational switch is correlated to a hypsochromic shift of the absorption as reported in the UV-Vis spectra (Figure S13). These experiments prove that the pH-driven vase-kite interconversion of the deeper quinoxaline cavitaund is easily triggered in solution in a reversible manner, allowing for a controllable guest uptake and release.

The behavior of **BenzoQxCav** in presence of TFA was monitored even by fluorescence spectroscopy. (**Figure S17**).



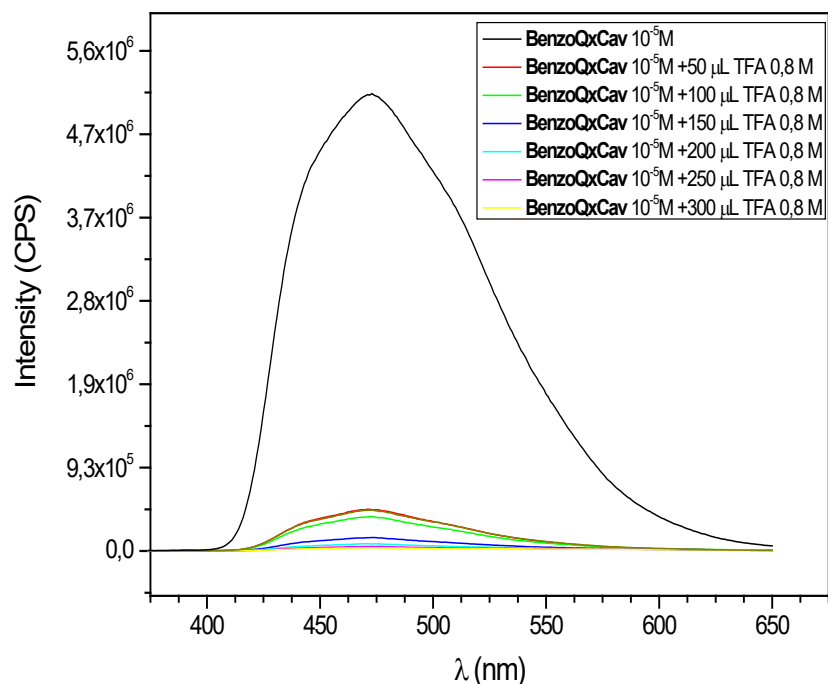


**Figure S17.** Changes of the Fluorescence Emission of **BenzoQxCav** ( $[\text{BenzoQxCav}] = 1.9 \cdot 10^{-5} \text{ M}$ ) in DCM upon addition of TFA.  $T = 25 \text{ }^\circ\text{C}$ .

The fluorescence emission spectra of a solution of **BenzoQxCav** ( $1.9 \cdot 10^{-5} \text{ M}$  in DCM at  $25 \text{ }^\circ\text{C}$ ) showed a maximum of emission at 472 nm. The effect of the first addition of 50  $\mu\text{L}$  of TFA (0.8 M in DCM) led to a drastic quench of the fluorescence emission, without any shift of the maximum emission peak, which was further reduced by the subsequent additions of TFA aliquots (Figure S17). The quenching is complete at 300  $\mu\text{L}$  addition. Addition of the equivalent amount of  $\text{NEt}_3$  restores the initial fluorescence (Figure 5b).

The conformational switch of **BenzoQxCav** from the vase form to the kite one was investigated further by  $^1\text{H-NMR}$  spectroscopy.

The addition of TFA to the NMR tube containing a solution of **BenzoQxCav** in  $\text{CDCl}_3$  led to the opening of the cavitand conformation in the kite form, as highlighted by the diagnostic methine shift from 5.49 to 3.90 ppm and the downfield shift of the benzoquinoxaline peaks in the aromatic region. (Figure S18, red spectrum).

The reversibility of the conformational switch from kite to vase was achieved after addition of an ammonia solution (Figure S18, blue spectrum), leading to the restore of the initial peak chemical shifts in the aromatic region.

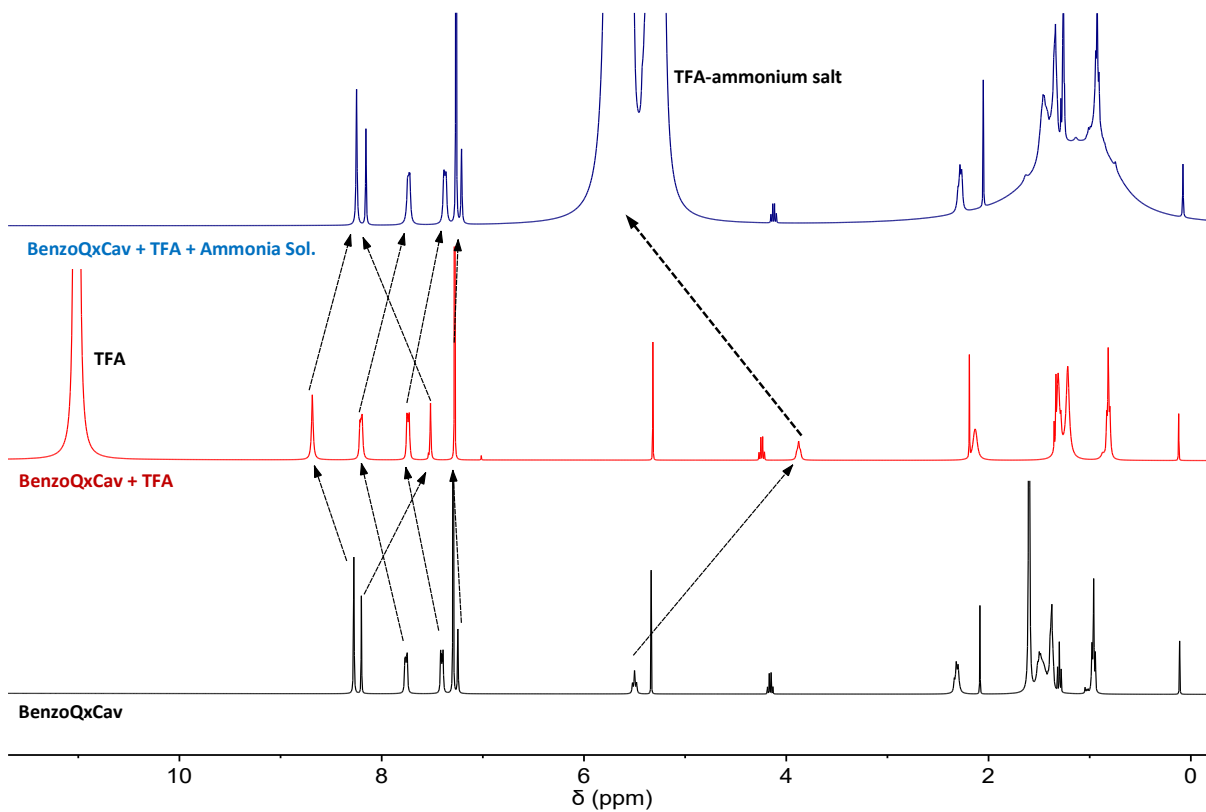


**Figure S18.** Conformational switch of **BenzoQxCav** ( $[\text{BenzoQxCav}] = 1.9 \cdot 10^{-3} \text{ M}$ ) in  $\text{CDCl}_3$  upon addition of TFA (31  $\mu\text{L}$ ) and ammonia solution (42  $\mu\text{L}$ ) monitored by  $^1\text{H-NMR}$  (400 MHz,  $T = 25^\circ\text{C}$ ).

## 14 SEM analysis of PAN-BenzoQxCav after use and regeneration

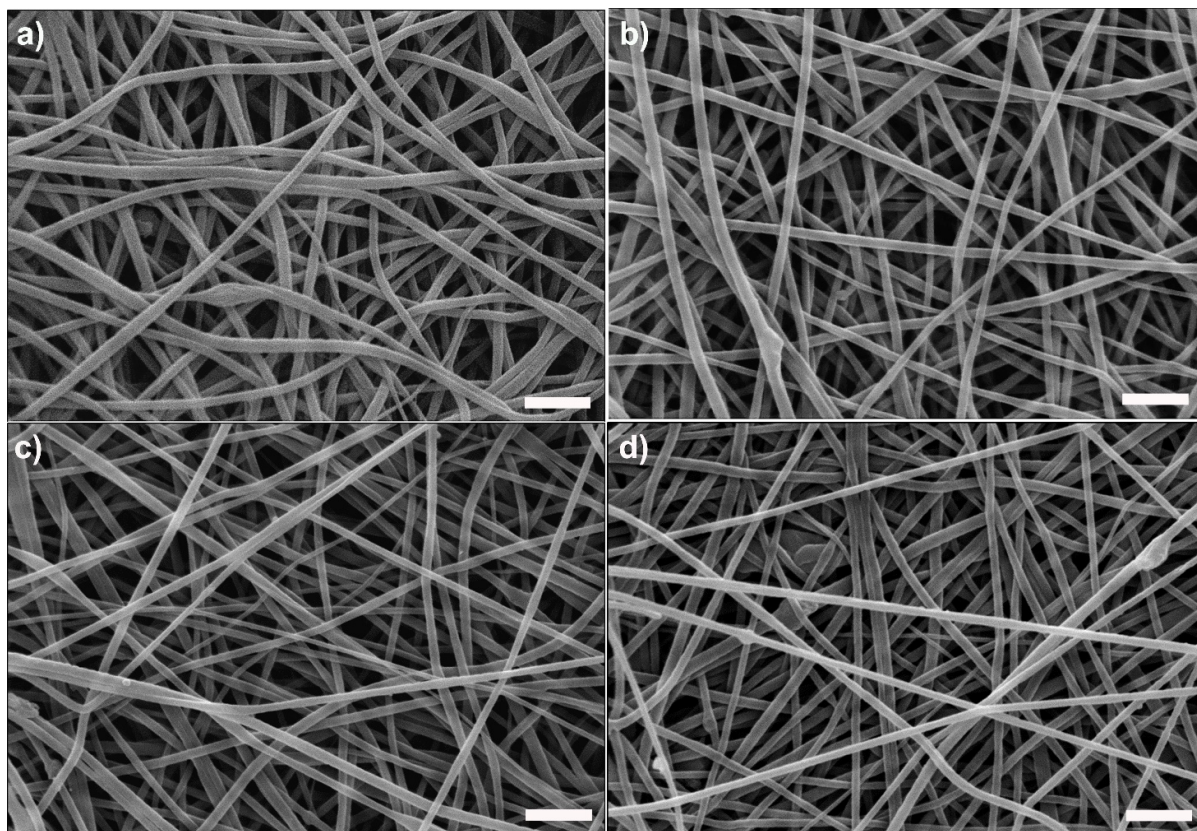


**Figure S19.** SEM micrographs of PAN-**BenzoQxCav** membrane after the first PAHs extraction cycle (a), followed by treatment with TFA aqueous solution (b) and treatment with ammonia aqueous solution (c). SEM analysis of the regenerated membrane after an additional cycle of PAHs extraction (d). Scale bars: 2  $\mu\text{m}$ .

## 15 Regeneration and reuse of the pristine PAN electrospun membranes

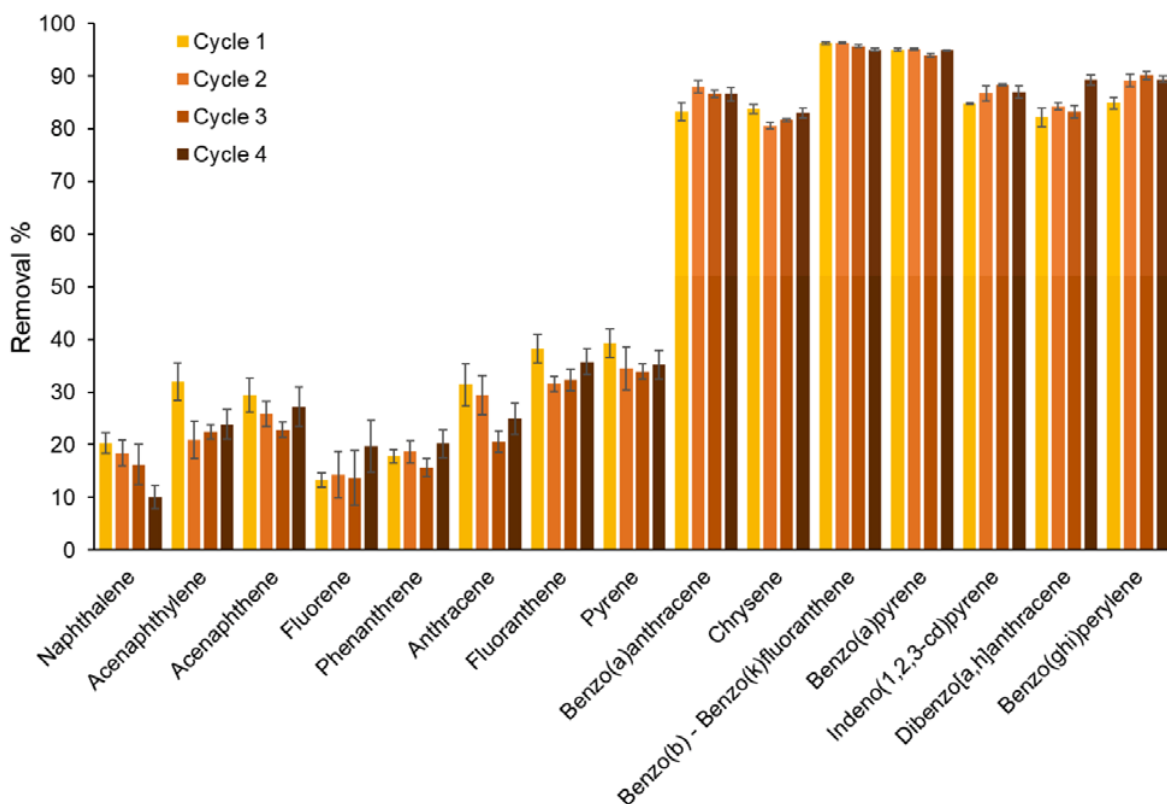


**Figure S20.** Removal capability of unfunctionalized PAN membranes after 4 regeneration steps.

## 16 References

- [1] L. Abis, E. Dalcanale, A. Du vosel, S. Sperala, *J. Org. Chem.* **1988**, *53*, 5475.
- [2] F. Beaulieu, C. Ouellet, E. H. Ruediger, M. Belema, Y. Qiu, X. Yang, J. Banville, J. R. Burke, K. R. Gregor, J. F. MacMaster, A. Martel, K. W. McIntyre, M. A. Pattoli, F. C. Zusi, D. Vyas, *Bioorganic Med. Chem. Lett.* **2007**, *17*, 1233.
- [3] *SADABS Bruker AXS; Madison, Wisconsin, USA, 2004; SAINT, Software Users Guide, Version 6.0; Bruker Analytical X-ray Systems, Madison, WI (1999). Sheldrick, G. M. SADABS v2.03: Area-Detector Absorption Correction. University of Göttingen, Germany, 1999.; 1999.*
- [4] A. Altomare, M. C. Burla, M. Camalli, G. L. Cascarano, C. Giacovazzo, A. Guagliardi, A. G. Moliterni, G. Polidori, R. Spagna, *J. Appl. Crystallogr.* **1999**, *32*, 115.
- [5] G. M. Sheldrick, A short history of SHELX. *Acta Crystallogr. Sect. A Found. Crystallogr.* **2008**, *64*, 112–122.
- [6] L. J. Farrugia, *J. Appl. Crystallogr.* **2012**, *45*, 849.

- [7] A. Celebioglu, F. Topuz, Z. I. Yildiz, T. Uyar, *ACS Omega* **2019**, *4*, 7850.
- [8] Y. Dai, J. Niu, L. Yin, J. Xu, Y. Xi, *J. Hazard. Mater.* **2011**, *192*, 1409.
- [9] J. R. Moran, J. L. Ericson, E. Dalcanale, J. A. Bryant, C. B. Knobler, D. J. Cram, *J. Am. Chem. Soc.* **1991**, *113*, 5707.
- [10] M. Torelli, F. Terenziani, A. Pedrini, F. Guagnini, I. Domenichelli, C. Massera, E. Dalcanale, *ChemistryOpen* **2020**, *9*, 261.
- [11] P. J. Skinner, A. G. Cheetham, A. Beeby, V. Gramlich, F. Diederich, *Helv. Chim. Acta* **2001**, *84*, 2146.